

Hunt for $X(17)$

Jun Jiang,^{1,*} Cong-Feng Qiao,^{2,†} and Yu-Han Zhao^{1,‡}

¹*School of Physics, Shandong University, Jinan, Shandong 250100, China*

²*School of Physical Sciences, University of Chinese Academy of Sciences, Beijing 100049, China*

(Dated: January 14, 2026)

Abstract

The 8Be anomaly reported by the Atomki experiments can be explained by the hypothesis of an $X(17)$ boson that interacts with electrons via the “Vector \pm Axial-vector” ($V \pm A$) interaction. Using existing experimental data, we derive constraints on the couplings of the $X(17)$ boson to electrons within this $V \pm A$ framework. With this setup, we attempt to identify $X(17)$ signals in the $e^+e^- \rightarrow X(17) \rightarrow e^+e^-$ process at the PADME experiment and in the $e^+e^- \rightarrow X(17)\gamma \rightarrow e^+e^-\gamma$ process at the BESIII experiment. Our findings indicate that observing the $X(17)$ signal at the PADME experiment is pessimistic, whereas the BESIII experiment may provide a definitive answer regarding the $X(17)$ hypothesis.

Key words: $X(17)$, $V \pm A$ coupling

* jiangjun87@sdu.edu.cn

† qiaocf@ucas.ac.cn.

‡ zyh329@mail.sdu.edu.cn

I. INTRODUCTION

The Standard Model (SM) explains the fundamental interactions between elementary particles almost perfectly. However, phenomena such as the matter-antimatter asymmetry, dark matter, hierarchy problem, strong charge-parity problem, and the nature of the Higgs boson, along with flavor anomalies, indicate that New Physics (NP) must exist and is concealed within the anomalies of the SM. These mysteries and experimental anomalies motivate physicists to extend the SM and explore new forces and mechanisms.

In 2016, Krasznahorkay *et al.* from Atomki reported the observation of an unexpected bump in the electron-positron angular correlations during the transition of the excited ${}^8Be^*$ nucleus to its ground state [1, 2]. They proposed that this bump arose from the production and subsequent decay of a neutral isoscalar particle with a mass of approximately 17 MeV into an electron-positron pair, which was named $X(17)$. In 2019, the same group investigated the energy-sum and angular correlation spectra of electron-positron pairs emitted during the transition of excited ${}^4He^*$ to its ground state, and observed a peak that could also be explained by the same particle [3–5]. In 2022, they discovered a similar anomaly in the transition of excited ${}^{12}C^*$ to its ground state, which could be well accounted for by the existence of the previously proposed hypothetical $X(17)$ particle [6]. In 2023, they further confirmed the existence of $X(17)$ in an experiment investigating the Giant Dipole Resonance (GDR) of ${}^8Be^*$ [7, 8].

Several other experiments have attempted to replicate the Atomki anomalies or search for $X(17)$ in new experimental setups. The VNU-UoS experiment reproduced the anomaly in ${}^8Be^*$ decay and confirmed the $X(17)$ resonance with a significance exceeding 4σ [9]. In contrast, the MEG-II experiment also repeated the ${}^8Be^*$ measurement but found no significant signal; instead, it derived an upper limit on the $X(17)$ production branching ratio relative to photon emission [10]. The PADME experiment at the Frascati DAΦNE LINAC searched for $X(17)$ using a positron beam impinging on a fixed target [11]. Within a beam energy range of 262 MeV to 296 MeV (corresponding to center-of-mass energies of $16.4 < \sqrt{s} < 17.4$ MeV), the production rates of the Bhabha scattering process $e^+e^- \rightarrow e^+e^-$ and the $e^+e^- \rightarrow \gamma\gamma$ process were measured. A significant deviation was observed at $\sqrt{s} = 16.90$ MeV, with a local significance of 2.5σ and a global significance of $(1.77 \pm 0.15)\sigma$.

Assuming pure vector coupling, an upper limit of $|\varepsilon_e^v| \lesssim 5.6 \times 10^{-4}$ was obtained for the Xee coupling at the 90% confidence level (C.L.). Further new experiments are on the way to search for $X(17)$ signals [12].

The Atomki anomalies have attracted significant interest from theoretical physicists in both nuclear and particle physics. Feng *et al.* proposed a protophobic fifth-force interpretation for the observed anomaly in 8Be nuclear transitions [13–15], which brought the Atomki anomaly to the forefront of the NP community. The most puzzling aspect of the Atomki anomalies is their extremely low energy scale, which is clearly outside the realm of Quantum Chromodynamics (QCD). No one anticipated that NP would manifest itself around 17 MeV. Wong argued that Quantum Electrodynamics (QED) mesons (quark-antiquark pairs interacting solely via QED) can explain the Atomki anomaly [16, 17]. Zhang *et al.* interpreted the anomaly using the nuclear transition form factor [18]. Subsequently, they found that $X(17)$ production is dominated by direct transitions induced by transverse and longitudinal electric dipoles as well as charge dipoles, without proceeding through any nuclear resonance with a smooth energy dependence that occurs for all proton beam energies above threshold [19]. Hayes *et al.* reexamined the angular correlations in the e^+e^- decay of $^8Be^*$ and found no evidence for $X(17)$ [20]. They found that the existence of a “bump” in the measured angular distribution was strongly dependent on the assumed M1/E1 ratio, which was a strong function of energy, while it was assumed to be a constant in the Atomki experiments. To date, numerous NP explanations have been shown to be invalid, while several proposed solutions remain viable, see Ref. [12] for a brief review.

Physicists have further attempted to derive constraints on the couplings of $X(17)$ to electrons and nucleons. In Refs. [13, 14], Feng *et al.* discuss a protophobic vector gauge boson interpretation of the 8Be anomaly. For a vector $X(17)$, they constrain the electron coupling strength ε_e^v to the range $2 \times 10^{-4} \lesssim |\varepsilon_e^v| \lesssim 1.4 \times 10^{-3}$, while the neutron coupling strength is constrained to $|\varepsilon_n^v| \lesssim 2.5 \times 10^{-2}$. Using a combined analysis of data samples collected in 2017 and 2018, the NA64 collaboration reports that the parameter region $1.2 \times 10^{-4} < |\varepsilon_e^v| < 6.8 \times 10^{-4}$ can be excluded at the 90% C.L. [21]. The PADME experiment has further refined this constraint, placing an upper limit of $|\varepsilon_e^v| \lesssim 5.6 \times 10^{-4}$ at the 90% C.L. [11]. As discussed in Ref. [22], the excess observed by PADME for the vector coupling is already in tension with constraints from two sources: the electron’s anomalous magnetic moment

(AMM), and the non-observation of exotic decays $\pi^+ \rightarrow e^+ \nu X(17)$ and $\mu^+ \rightarrow e^+ \bar{\nu}_\mu \nu_e X(17)$ at the SINDRUM experiment. In Ref. [23], Krasnikov points out that the NA64 bounds on the Xee coupling, combined with the latest values of the electron's AMM [24], exclude pure vector or axial-vector couplings of the $X(17)$ boson to electrons at the 90% C.L.; however, mixed “Vector \pm Axial-vector” ($V \pm A$) couplings remain viable. For the $V \pm A$ coupling to electrons, Barducci and Toni discuss constraints on the parameter $\sqrt{(\varepsilon_e^v)^2 + (\varepsilon_a^v)^2}$ extracted from multiple experiments in Appendix F of Ref. [25]. We will compare our results with theirs in detail in Section II.

In this paper, we aim to identify the $X(17)$ signal under the assumption that $X(17)$ couples to electrons via the $V \pm A$ interaction, focusing on the processes $e^+ e^- \rightarrow X(17) \rightarrow e^+ e^-$ and $e^+ e^- \rightarrow X(17)\gamma \rightarrow e^+ e^- \gamma$. In Section II, we introduce the $V \pm A$ model and present constraints on the coupling strength of $X(17)$ to electrons derived from current experimental data. In Section III, we discuss the feasibility of identifying $X(17)$ in the Bhabha scattering process $e^+ e^- \rightarrow e^+ e^-$ at the PADME experiment. In Section IV, we revisit the $e^+ e^- \rightarrow X(17)\gamma \rightarrow e^+ e^- \gamma$ process at the BESIII experiment, and elaborate on how to identify the $X(17)$ bump after accounting for smearing effects. The final section is dedicated to a summary and prospects.

II. CONSTRAINTS ON “ $V \pm A$ ” MODEL

In this section, we introduce a spin-1 $X(17)$ model with “Vector \pm Axial-vector” ($V \pm A$) couplings to electrons, which is proposed to explain the Atomki anomalies. We first present the model in subsection II A, followed by a discussion of constraints on the coupling strength of the $X(17)$ boson to electrons in subsections II B and II C.

A. “Vector \pm Axial-vector” Model

In our previous work [26, 27], we adopted the “ $V - A$ ” model to describe the interaction between the $X(17)$ boson and fermions, and made a rough assumption of equal vector and axial-vector coupling strengths in the numerical calculations. In the present manuscript, we extend this hypothesis to the general “ $V \pm A$ ” model, where the vector and axial-vector

coupling strengths are allowed to vary within the range constrained by current experimental data.

The general Lagrangian for the $X(17)$ boson can be formulated as

$$\mathcal{L}_X = -\frac{1}{4}X_{\mu\nu}X^{\mu\nu} + \frac{1}{2}m_X^2X_\mu X^\mu - \sum_f e\bar{f}\gamma_\mu(\varepsilon_f^v - \varepsilon_f^a\gamma_5)fX^\mu, \quad (1)$$

where the new boson $X(17)$ with mass m_X has the field strength $X_{\mu\nu} \equiv \partial_\mu X_\nu - \partial_\nu X_\mu$ and couples to fermions via vector/axial-vector currents. The coupling strengths, denoted $\varepsilon_f^{v/a}$, are given in units of the electronic charge e . Here, the coupling parameters $\varepsilon_f^{v/a}$ can take either positive or negative values, implying that the interaction exhibits “ $V \pm A$ ” coupling to the fermion f . In the present manuscript, we focus exclusively on the couplings of the hypothetical $X(17)$ boson to electrons, which has already been implicated by several Atomki experiments.

The scalar $X(17)$ hypothesis has been excluded by parity conservation in the Atomki 8Be experiment, while a pseudoscalar state can only explain the 8Be and 4He anomalies, not the ${}^{12}C$ one [25]. In Ref. [23], Krasnikov argues that the combination of results from the latest NA64 experiment [21] and the recent value of the electron’s anomalous magnetic moment (AMM) [24] excludes pure vector and pure axial-vector couplings of the $X(17)$ boson to electrons at the 90% C.L. However, the model with “ $V \pm A$ ” interaction remains viable and can further account for both the electron and muon AMMs.¹ We discuss constraints on the coupling of the $X(17)$ boson to electrons from the Atomki experiments, the electron’s AMM, the beam dump experiments, and KLOE-2 experiment in Sec. II B. In Sec. II C, we present the viable regions of the Xee coupling for the “ $V \pm A$ ” model.

B. Constraints on Xee coupling

1. Atomki Experiments

In 2016, Krasznahorkay *et al.* reported the production of a neutral particle X , which subsequently decays to e^+e^- via internal pair creation, along with its mass and the ratio of

¹ The latest analysis of the muon’s AMM indicates that there is no tension between the Standard Model (SM) prediction [28] and experimental results [29] at the current level of precision.

decay widths [1],

$$m_X = 16.7 \pm 0.35(\text{stat.}) \pm 0.5(\text{sys.}) \text{ MeV}, \quad (2)$$

$$\frac{\Gamma(^8\text{Be}^* \rightarrow ^8\text{Be}X) \text{Br}(X \rightarrow e^+e^-)}{\Gamma(^8\text{Be}^* \rightarrow ^8\text{Be}\gamma)} = 5.8 \times 10^{-6}. \quad (3)$$

Later, they updated the measurement of its mass to $m_X = 17.01 \pm 0.16$ MeV and the branching fraction ratio in Eq. (3) to $(6 \pm 1) \times 10^{-6}$ [2, 4]. Using $\Gamma(^8\text{Be}^* \rightarrow ^8\text{Be}\gamma) = 1.9 \pm 0.4$ eV [30] and further assuming $\text{Br}(X \rightarrow e^+e^-) \approx 1$, we obtain $\Gamma(^8\text{Be}^* \rightarrow ^8\text{Be}X) = (1.1 \pm 0.31) \times 10^{-5}$ eV. The radiative transition of ${}^8\text{Be}^*$ ($J^P = 1^+$) to the ground state ${}^8\text{Be}$ ($J^P = 0^+$) implies that $X(17)$ can be either a $J^P = 1^+$ boson (with orbital angular momentum 0), or a $J^P = 0^-$ boson (with orbital angular momentum 1). The scalar $X(17)$ hypothesis has been excluded. Very recently, Arias-Aragón *et al.* combined results from the PADME experiment with Atomki nuclear physics results and derived a value of $m_X = 16.88 \pm 0.05$ MeV for the $X(17)$ mass [9], which will be adopted throughout this paper.

In the rest frame of the ${}^8\text{Be}^* \rightarrow {}^8\text{Be}X$ decay², the $X(17)$ boson is produced with a velocity of $v \approx 0.37c$. One can then estimate the decay length for the $X \rightarrow e^+e^-$ process as

$$L = \frac{\hbar \times c}{\Gamma(X \rightarrow e^+e^-)} \times \frac{v}{\sqrt{1 - v^2}}, \quad (4)$$

where \hbar is the reduced Planck constant. Here, we assume that the $X \rightarrow e^+e^-$ decay is saturated. Within our “ $V \pm A$ ” model, the decay width of the X boson to electron-positron pairs can be formulated as follows, up to an error of $\mathcal{O}\left(\left(\frac{m_e}{m_X}\right)^2\right) \approx 0.1\%$,

$$\Gamma(X \rightarrow e^+e^-) \approx \frac{\alpha m_X}{3} ((\varepsilon_e^v)^2 + (\varepsilon_e^a)^2), \quad (5)$$

where α is the fine structure constant. This implies that the vector and axial-vector couplings make nearly identical contributions, aside from differences in their coupling parameters. This approximate expression is sufficiently accurate, and its distinction from the exact result is negligible, which we have illustrated in our previous work [26, 27].

According to the setup of the Atomki experiments [31], the travel length of the $X(17)$ boson must be less than approximately 5 cm. Numerically, imposing the constraint $L \leq 5$ cm on the decay length, the ${}^8\text{Be}$ anomaly experiment implies $(\varepsilon_e^v)^2 + (\varepsilon_e^a)^2 \gtrsim 3.8 \times 10^{-11}$.

² In the laboratory frame, the produced ${}^8\text{Be}^*$ state moves nonrelativistically with a velocity of $0.006c$, where c is the speed of light. Thus, assuming the ${}^8\text{Be}^*$ rest frame is appropriate.

If we assume that the X boson decays shortly after its production and further impose the stricter constraint $L \leq 1$ cm, we obtain

$$(\varepsilon_e^v)^2 + (\varepsilon_e^a)^2 \gtrsim 1.9 \times 10^{-10}, \quad (6)$$

For the pure vector coupling case (setting $\varepsilon_e^a = 0$), we derive $|\varepsilon_e^v| \gtrsim 1.4 \times 10^{-5}$, which is consistent with the estimate in Ref. [13] when adopting $m_X = 17$ MeV.

In 2019, Krasznahorkay *et al.* reported new evidence supporting the existence of the hypothetical $X(17)$ boson in the decay of the excited ${}^4\text{He}^*$ state to its ground state [3]. The ${}^4\text{He}^*(J^P = 0^-) \rightarrow {}^4\text{He}(0^+)$ transition implies that $X(17)$ can be either a $J^P = 1^+$ boson (with orbital angular momentum 1) or a $J^P = 0^-$ boson (with orbital angular momentum 0). Again, the scalar $X(17)$ hypothesis is excluded. Subsequently, in 2021, they bombarded ${}^3\text{H}$ with protons of energies 510, 610, and 900 keV to populate the first and second excited states of ${}^4\text{He}^*$ [5], and once more observed such anomalous signals of $X(17)$. The derived average values for the mass of $X(17)$ and the decay width ratio are

$$m_X = 16.94 \pm 0.12(\text{stat}) \pm 0.21(\text{sys}) \text{ MeV}, \quad (7)$$

$$\frac{\Gamma({}^4\text{He}^* \rightarrow {}^4\text{He}X) \text{ Br}(X \rightarrow e^+e^-)}{\Gamma({}^4\text{He}^* \rightarrow {}^4\text{He}\gamma)} = (5.1 \pm 0.13) \times 10^{-6}. \quad (8)$$

In the rest frame of the ${}^4\text{He}^* \rightarrow {}^4\text{He}X$ decay ³, the velocity of $X(17)$ is $v \approx 0.59c$. Imposing the constraint $L \leq 5$ cm on the decay length, one can estimate a lower limit of $(\varepsilon_e^v)^2 + (\varepsilon_e^a)^2 \gtrsim 7.0 \times 10^{-11}$. For a stricter decay length constraint of $L \leq 1$ cm, one obtains

$$(\varepsilon_e^v)^2 + (\varepsilon_e^a)^2 \gtrsim 3.5 \times 10^{-10}. \quad (9)$$

These two lower limits (for $L \leq 5$ cm and $L \leq 1$ cm) in the ${}^4\text{He}^*$ case are approximately twice those derived in the ${}^8\text{Be}^*$ case, respectively. For the pure vector or pure axial-vector coupling scenario, imposing the $L \leq 1$ cm constraint requires $|\varepsilon_e^v|$ or $|\varepsilon_e^a|$ to be greater than approximately 1.9×10^{-5} .

In 2022, Krasznahorkay *et al.* further reported a new anomaly supporting the existence and vector character of the hypothetical $X(17)$ boson [6]. They bombarded ${}^{11}\text{B}$ with protons of five energies in the range of 1.5 – 2.5 MeV to study the transition ${}^{12}\text{C}^*(1^-) \rightarrow {}^{12}\text{C}(0^+)$,

³ In the laboratory frame, the produced ${}^4\text{He}^*$ state moves nonrelativistically with a velocity of $0.011c$ for a proton beam energy of 900 keV. Thus, the assumption of the ${}^4\text{He}^*$ rest frame is appropriate.

which implies that $X(17)$ can be either a $J^P = 1^-$ boson (with orbital angular momentum 1) or a $J^P = 0^+$ boson (with orbital angular momentum 0). The pseudoscalar $X(17)$ hypothesis is excluded. The average values of the $X(17)$ mass and the decay width ratio are

$$m_X = 17.03 \pm 0.11(\text{stat}) \pm 0.20(\text{sys}) \text{ MeV}, \quad (10)$$

$$\frac{\Gamma(^{12}\text{C}^* \rightarrow ^{12}\text{C}X) \text{Br}(X \rightarrow e^+e^-)}{\Gamma(^{12}\text{C}^* \rightarrow ^{12}\text{C}\gamma)} = (3.6 \pm 0.3) \times 10^{-6}. \quad (11)$$

In the rest frame of the $^{12}\text{C}^* \rightarrow ^{12}\text{C}X$ decay ⁴, the velocity of $X(17)$ is $v \approx 0.20c$. Imposing the constraint $L \leq 5$ cm on the decay length, one can then estimate a lower limit of $(\varepsilon_e^v)^2 + (\varepsilon_e^a)^2 \gtrsim 2.0 \times 10^{-11}$. For a stricter decay length constraint of $L \leq 1$ cm, one obtains

$$\boxed{(\varepsilon_e^v)^2 + (\varepsilon_e^a)^2 \gtrsim 9.8 \times 10^{-11}}. \quad (12)$$

These two lower limits (for $L \leq 5$ cm and $L \leq 1$ cm) in the $^{12}\text{C}^*$ case are approximately half of those derived in the $^8\text{Be}^*$ case, respectively. In the subsequent discussion, we adopt Eq. (12) as the constraint from the Atomki experiments, so it is enclosed in a box. For the pure vector or pure axial-vector coupling scenario, this constraint requires $|\varepsilon_e^v|$ or $|\varepsilon_e^a|$ to be greater than approximately 9.9×10^{-6} . In Eq. (F.6) of Ref. [25], Barducci and Toni derive a constraint of $(\varepsilon_e^v)^2 + (\varepsilon_e^a)^2 \gtrsim 9 \times 10^{-14}$ by assuming the prompt and saturated decay of $X(17) \rightarrow e^+e^-$ in the Atomki detector.

2. Electron Anomalous Magnetic Momentum

Since the hypothetical $X(17)$ boson couples to electrons, it will contribute to the electron's anomalous magnetic moment (AMM), defined as $a_e \equiv (g_e - 2)/2$. In 2022, an improved determination of the electron AMM was reported [32],

$$a_e^{\text{exp}} = 0.00115965218059 (13), \quad (13)$$

which is 2.2 times more accurate than the 2008 measurement [33]. When compared with the 2018 SM prediction [24],

$$a_e^{\text{SM}} = 0.00115965218161 (23), \quad (14)$$

⁴ In the laboratory frame, the produced $^{12}\text{C}^*$ state moves nonrelativistically with a velocity of $0.005c$. Thus, the assumption of the $^{12}\text{C}^*$ rest frame is appropriate.

there is a -3.9σ discrepancy between the experimental measurement and the SM prediction for the electron AMM, given by

$$\Delta a_e \equiv a_e^{\text{exp}} - a_e^{\text{SM}} = (-1.02 \pm 0.26) \times 10^{-12}. \quad (15)$$

Within the “ $V \pm A$ ” framework, the $X(17)$ boson contributes to the electron’s AMM via the leading one-loop triangle diagram [34], with the contribution given by

$$a_e^X = \frac{\alpha}{3\pi} \left(\frac{m_e}{m_X} \right)^2 [(\varepsilon_e^v)^2 - 5(\varepsilon_e^a)^2]. \quad (16)$$

To diminish the -3.9σ discrepancy between the experimental measurement and the SM prediction, i.e. requiring $\Delta a_e \lesssim a_e^X \lesssim 0$, we derive the following constraint

$$(-1.4 \pm 0.4) \times 10^{-6} \lesssim (\varepsilon_e^v)^2 - 5(\varepsilon_e^a)^2 \lesssim 0. \quad (17)$$

Adopting the 2008 measurement of the electron’s AMM yields a bound consistent with the result in Ref. [23]. For the pure vector coupling scenario, the $X(17)$ boson would exacerbate the electron AMM discrepancy. In contrast, for the pure axial-vector coupling scenario, one can deduce the constraint on the coupling parameter, $|\varepsilon_e^a| \lesssim (5.4 \pm 0.7) \times 10^{-4}$.

3. Beam Dump Experiments

In beam dump experiments, the $X(17)$ boson is produced via initial- or final-state radiation from a single electron impinging on a fixed target with atomic number Z , a process known as the bremsstrahlung reaction $e^-Z \rightarrow e^-ZX$. When considering the “ $V \pm A$ ” interaction between X and electrons in this process, the squared amplitudes are proportional to the coupling parameters solely through the combination $(\varepsilon_e^v)^2 + (\varepsilon_e^a)^2$, up to an error of $\mathcal{O}\left(\left(\frac{m_e}{m_X}\right)^2\right) \approx 0.1\%$. More specifically, in the Dirac trace of the closed electron loop within the squared amplitudes, the term $(\varepsilon_e^v + \varepsilon_e^a \gamma_5)$ must commute an odd number of times across $(\gamma^\mu + m_e)$ or γ^μ matrices to contract with its complex conjugate term $(\varepsilon_e^v - \varepsilon_e^a \gamma_5)$. Thus, in the squared amplitudes, the $m_e \rightarrow 0$ limit yields two contributions: the combined term $(\varepsilon_e^v)^2 + (\varepsilon_e^a)^2$ and the interference term $\varepsilon_e^v \varepsilon_e^a$. However, terms proportional to $\varepsilon_e^v \varepsilon_e^a$ always contain a single γ^5 in the Dirac trace and therefore vanish upon summation.

Recently, the NA64 collaboration has conducted multiple searches for the $X(17)$ boson and set constraints on the Xee coupling parameter, i.e. $\sqrt{(\varepsilon_e^v)^2 + (\varepsilon_e^a)^2}$ under the assumption

of a “ $V \pm A$ ” interaction with electrons, up to an error of $\mathcal{O}\left(\left(\frac{m_e}{m_X}\right)^2\right)$. In 2018, the NA64 collaboration first excluded the region $1.3 \times 10^{-4} < \sqrt{(\varepsilon_e^v)^2 + (\varepsilon_e^a)^2} < 4.2 \times 10^{-4}$ at the 90% C.L. [35]. Subsequently, in 2019, a combined analysis of the data samples collected in 2017 and 2018 allowed them to extend the exclusion region to $1.2 \times 10^{-4} < \sqrt{(\varepsilon_e^v)^2 + (\varepsilon_e^a)^2} < 6.8 \times 10^{-4}$ at the 90% C.L. [21].⁵ In 2020, the NA64 collaboration presented an independent analysis [36] that confirmed the 2019 result reported in Ref. [21]. In 2021, assuming $X(17)$ is a pseudoscalar boson, they excluded the range $(2.1 \sim 3.2) \times 10^{-4}$ [37].

Additional constraints exist from other beam dump experiments that utilize the bremsstrahlung reaction to search for low-mass dark bosons, namely the E137, E141, and E774 experiments. In the mass region around 17 MeV, the combined results of the E137 and E141 experiments have excluded the region $8 \times 10^{-8} \lesssim \sqrt{(\varepsilon_e^v)^2 + (\varepsilon_e^a)^2} \lesssim 3 \times 10^{-4}$ [38].⁶

In summary, at the 90% C.L. and up to an error of $\mathcal{O}\left(\left(\frac{m_e}{m_X}\right)^2\right)$, beam dump experiments have excluded the range $8 \times 10^{-8} \lesssim \sqrt{(\varepsilon_e^v)^2 + (\varepsilon_e^a)^2} \lesssim 6.8 \times 10^{-4}$ for $m_X = 17$ MeV. Thus, we derive a lower limit on the Xee coupling strength,

$$(\varepsilon_e^v)^2 + (\varepsilon_e^a)^2 \gtrsim 4.6 \times 10^{-7}. \quad (18)$$

For the pure vector or pure axial-vector scenario, the same constraint applies to $|\varepsilon_e^v|$ or $|\varepsilon_e^a|$, which requires these parameters to be greater than approximately 6.8×10^{-4} . The coupling combination $(\varepsilon_e^v)^2 + (\varepsilon_e^a)^2$ could also be smaller than 6.4×10^{-15} ; however, this value is extremely small, so we do not discuss the feasibility of searching for $X(17)$ in this region.

4. KLOE-2 Experiment

The KLOE-2 collaboration searched for a low-mass vector boson U in the process $e^+e^- \rightarrow U\gamma$ with $U \rightarrow e^+e^-$ using the KLOE₍₃₎ dataset, and set an upper bound on the Xee coupling

⁵ In Eq. (F.5) of Ref. [25], it is claimed that the NA64 experiments yield the constraint $\sqrt{(\varepsilon_e^v)^2 + (\varepsilon_e^a)^2} \gtrsim 3.6 \times 10^{-5}$, which contradicts the NA64 results [21, 35]. Notably, this inconsistent limit affects our final constraints.

⁶ The data were extracted from Fig. 1 in Ref. [38] using WebPlotDigitizer [39]. In Eq. (F.4) of Ref. [25], the lower exclusion limit is reported as 1.1×10^{-8} , which differs from our result by a factor of approximately eight. This discrepancy arises because they extracted E141 experiment data from Figs. 2 and 3 of Ref. [40], which differ slightly from Fig. 1 in Ref. [38]. Notably, this inconsistent limit does not affect our final constraints.

around 17 MeV at the 90% C.L. [41],⁷

$$(\varepsilon_e^v)^2 + (\varepsilon_e^a)^2 \lesssim 4 \times 10^{-6}. \quad (19)$$

In Sec. IV A, we will demonstrate that, within the “ $V \pm A$ ” framework, the cross section of the $e^+e^- \rightarrow U\gamma$ process is proportional to the coupling parameters solely through the combination $(\varepsilon_e^v)^2 + (\varepsilon_e^a)^2$, up to an error of $\mathcal{O}\left(\left(\frac{m_e}{m_X}\right)^2\right)$. For the pure vector or pure axial-vector scenario, the same upper bound applies to $|\varepsilon_e^v|$ or $|\varepsilon_e^a|$, which is approximately 2×10^{-3} .

C. Survival for Xee Coupling

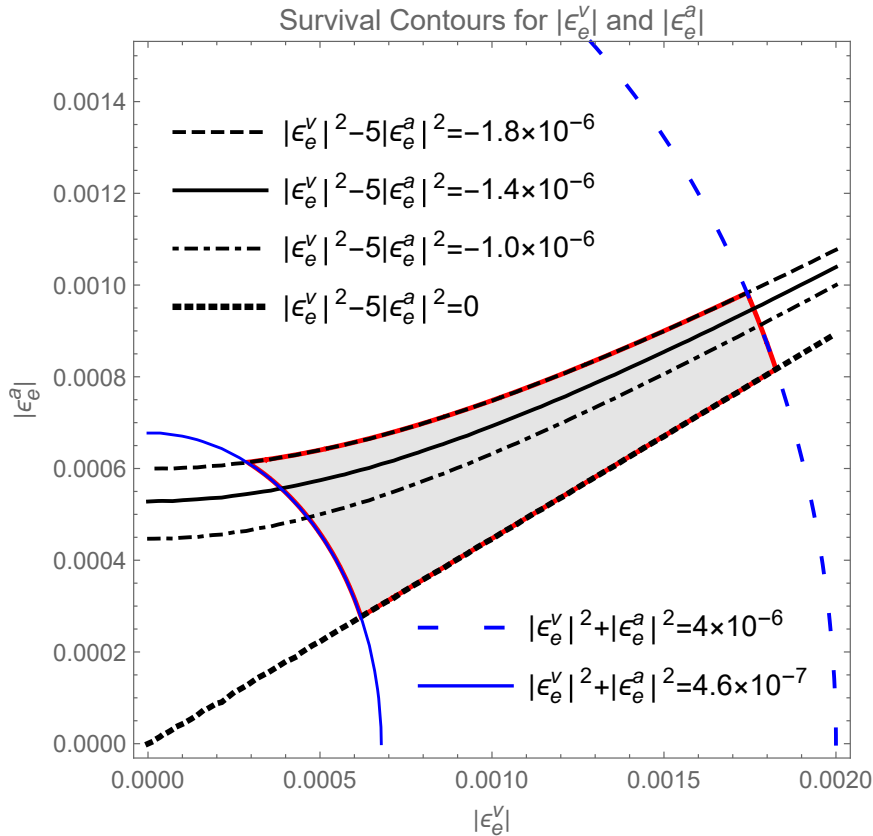


FIG. 1: Contour curves of the survived region for the coupling parameters $|\varepsilon_e^v|$ and $|\varepsilon_e^a|$ in the “ $V \pm A$ ” model. The boundary of this survived region is marked by the red curve.

⁷ The data were extracted from Fig. 7 in Ref. [41] using WebPlotDigitizer [39]. In Eq. (F.2) of Ref. [25], it is claimed that the KLOE experiment yields the constraints $\sqrt{(\varepsilon_e^v)^2 + (\varepsilon_e^a)^2} \lesssim 6.1 \times 10^{-4}$ (or equivalently $(\varepsilon_e^v)^2 + (\varepsilon_e^a)^2 \lesssim 3.7 \times 10^{-7}$), which contradicts the data presented in Fig. 7 of Ref. [41] and differs from our result by a factor of ten. Notably, this inconsistent limit affects our final constraints.

To summarize the discussions in Sec. II B, the Atomki experiments, along with the beam dump experiments (E141, E774) and the NA64 collaboration, set lower bounds on the coupling combination $(\varepsilon_e^v)^2 + (\varepsilon_e^a)^2$, while the KLOE-2 experiment establishes an upper bound on this quantity. Additionally, the electron's AMM imposes a constraint on $(\varepsilon_e^v)^2 - 5(\varepsilon_e^a)^2$ to mitigate the existing anomaly. By combining Eqs. (12, 17, 18) and (19), we derive the survived region for the coupling parameters $|\varepsilon_e^v|$ and $|\varepsilon_e^a|$ within the “ $V \pm A$ ” model,

$$4.6 \times 10^{-7} \lesssim (\varepsilon_e^v)^2 + (\varepsilon_e^a)^2 \lesssim 4 \times 10^{-6},$$

$$(-1.4 \pm 0.4) \times 10^{-6} \lesssim (\varepsilon_e^v)^2 - 5(\varepsilon_e^a)^2 \lesssim 0.$$

(20)

This survived region is illustrated as contour curves in Fig. 1, where the boundary of the viable Xee coupling is marked by the red curve.

For the pure vector and pure axial-vector models, their respective survived regions are also derived as follows,

$$\text{Pure } V \text{ survival: Disfavored by the electron's AMM,} \quad (21)$$

$$\text{Pure } A \text{ survival: } 6.8 \times 10^{-4} \lesssim |\varepsilon_e^a| \lesssim (5.3 \pm 0.8) \times 10^{-4}. \quad (22)$$

For the pure vector coupling scenario, the introduction of $X(17)$ would further exacerbate the electron AMM discrepancy Δa_e given in Eq. (15). For the pure axial-vector coupling scenario, one finds that the upper and lower bounds are nearly overlapping. The uncertainty in the upper bound originates from the uncertainty of the electron AMM measurement.

III. $e^+e^- \rightarrow X(17) \rightarrow e^+e^-$ AT PADME

Very recently, the PADME experiment at the Frascati DAΦNE LINAC searched for $X(17)$ using a positron beam incident on a fixed target [11]. They measured the production rates of Bhabha scattering ($e^+e^- \rightarrow e^+e^-$) and the two-photon process ($e^+e^- \rightarrow \gamma\gamma$) over a beam energy range of 262–296 MeV, corresponding to center-of-mass energies of $16.4 < \sqrt{s} < 17.4$ MeV. This measurement was conducted during a three-month data-taking period in late 2022, covering the relevant mass region indicated by the multiple Atomki experiments. The most significant deviation was observed at $\sqrt{s} \simeq 16.90$ MeV, with a local significance of 2.5σ and a global significance of $(1.77 \pm 0.15)\sigma$. Assuming pure vector coupling, an upper

limit of $|\varepsilon_e^v| \lesssim 5.6 \times 10^{-4}$ was established at the 90% C.L. In this section, we discuss the prospects of identifying $X(17)$ in Bhabha scattering ($e^+e^- \rightarrow e^+e^-$) within the $V \pm A$ model, incorporating the constraints derived in Sec. II C. For the subsequent numerical calculations, we adopt the average $X(17)$ mass $m_X = 16.88 \pm 0.05$ MeV [9] and a center-of-mass energy of $\sqrt{s} = 16.9 \pm 0.5$ MeV.

A. $e^+e^- \rightarrow X(17)$

For the production process $e^+e^- \rightarrow X(17)$, the total cross section takes the following simple form,

$$\sigma = \frac{2\pi^2\alpha}{s\sqrt{s(s-4m_e^2)}} \left(s \left((\varepsilon_e^a)^2 + (\varepsilon_e^v)^2 \right) + 2m_e^2 \left((\varepsilon_e^v)^2 - \left(3 - \frac{s}{m_X^2} \right) (\varepsilon_e^a)^2 \right) \right) \delta \left(1 - \frac{m_X}{\sqrt{s}} \right), \quad (23)$$

where the δ function arises from the one-particle phase space. In the limit $m_e^2 \ll s$, the cross section simplifies to

$$\sigma = \frac{2\pi^2\alpha}{s} \left((\varepsilon_e^a)^2 + (\varepsilon_e^v)^2 \right) \delta \left(1 - \frac{m_X}{\sqrt{s}} \right) + \mathcal{O} \left(\left(\frac{m_e}{\sqrt{s}} \right)^2 \right). \quad (24)$$

B. $X \rightarrow e^+e^-$

We are confident that $X(17)$ can decay into electron-positron pairs, which means its signal bump can be reconstructed in the invariant mass spectrum of electron-positron pairs. The decay width of $X \rightarrow e^+e^-$ is given in Eq. (5). Using the bounds on the coupling parameters $|\varepsilon_e^v|$ and $|\varepsilon_e^a|$ shown in Fig. 1, we can estimate the decay width of $X \rightarrow e^+e^-$ within the “ $V \pm A$ ” model, as presented in Fig. 2. The upper and lower limits of the decay width are

$$0.018 \text{ eV} \lesssim \Gamma(X \rightarrow e^+e^-) \lesssim 0.16 \text{ eV}, \quad (25)$$

where these limits correspond to the following coupling parameter values,

$$\begin{aligned} (|\varepsilon_e^v|, |\varepsilon_e^a|)_{\max}^{\Gamma \rightarrow e^+e^-} &\simeq (1.8, 0.82) \times 10^{-3}, \\ (|\varepsilon_e^v|, |\varepsilon_e^a|)_{\min}^{\Gamma \rightarrow e^+e^-} &\simeq (2.7, 6.1) \times 10^{-4}. \end{aligned} \quad (26)$$

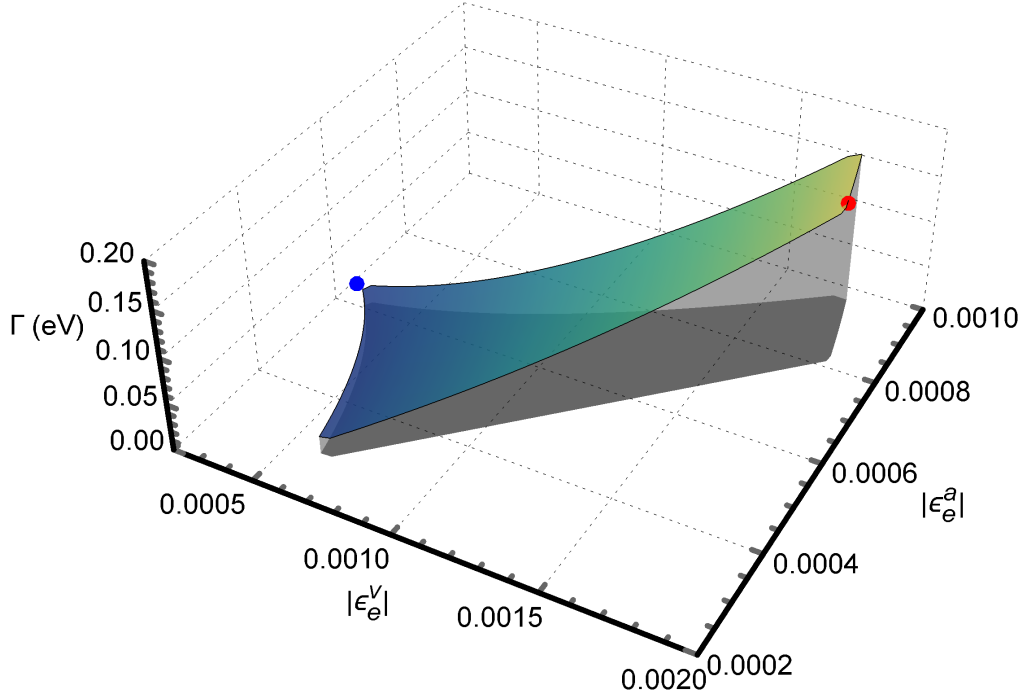


FIG. 2: The decay width of $X \rightarrow e^+e^-$ as a function of the coupling parameters $|\varepsilon_e^v|$ and $|\varepsilon_e^a|$. The parameters $|\varepsilon_e^{v/a}|$ are constrained within the red region shown in Fig. 1. The red and blue spots denote the points corresponding to the maximum and minimum decay width values, respectively.

If we further assume that the branching fraction of this decay mode is approximately saturated, the lifetime of the $X(17)$ boson in its rest frame would be $4.0 \sim 36$ fs. For the subsequent numerical calculations, we adopt the median value of the decay width, $\Gamma(X \rightarrow e^+e^-) \approx 0.089$ eV.

C. $e^+e^- \rightarrow X(17) \rightarrow e^+e^-$

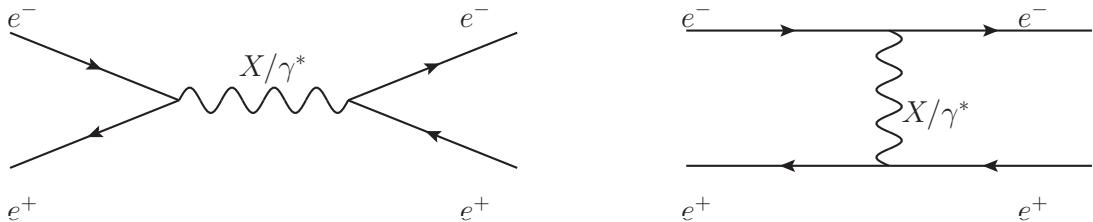


FIG. 3: The Feynman diagrams for the $e^+e^- \rightarrow X(17)/\gamma^* \rightarrow e^+e^-$ processes.

Feynman diagrams for the signal (S) and background (B) processes, namely $e^+e^- \rightarrow X(17) \rightarrow e^+e^-$ and $e^+e^- \rightarrow \gamma^* \rightarrow e^+e^-$ are shown in Fig. 3. Under the approximation $m_e^2 \ll s$, the differential cross section for the Bhabha scattering background process takes the following simple form,

$$\frac{d\sigma_B}{d\cos\theta} = \frac{\pi\alpha^2}{2s} \left(\frac{3 + \cos^2\theta}{1 - \cos\theta} \right)^2 + \mathcal{O}\left(\left(\frac{m_e}{\sqrt{s}}\right)^2\right). \quad (27)$$

The corresponding total cross section is

$$\begin{aligned} \sigma_B &= \frac{\pi\alpha^2}{2s} (I(\theta_2) - I(\theta_1)) + \mathcal{O}\left(\left(\frac{m_e}{\sqrt{s}}\right)^2\right), \\ I(\theta) &\equiv \frac{\cos^3\theta}{3} + \cos^2\theta + 9\cos\theta + \frac{16}{1 - \cos\theta} + 16\log(\cos\theta - 1) - \frac{31}{3}, \end{aligned} \quad (28)$$

which diverges as $\cos\theta \rightarrow 1$. Specifically, the divergence behaves as

$$\sigma_B \rightarrow \frac{8\pi\alpha^2}{s} \left(\frac{1}{1 - \cos\theta} + \log\left(\frac{1 - \cos\theta}{2}\right) + \frac{2}{3} \right) \quad \text{for } \cos\theta \rightarrow 1. \quad (29)$$

Notably, the approximate result in Eq. (28) is not reliable due to this divergence. For the signal process, the differential cross section is given by

$$\begin{aligned} \frac{d\sigma_S}{d\cos\theta} &= \frac{\pi\alpha^2 s}{2(s - m_X^2)^2(s + 2m_X^2 - s\cos\theta)^2} \left(((\varepsilon_e^v)^4 + (\varepsilon_e^a)^4) \right. \\ &\quad \times (s^2(\cos^2\theta + 3)^2 - 6m_X^2 s(\cos^2\theta + 3)(\cos\theta + 1) + 2m_X^4(\cos\theta(5\cos\theta + 6) + 9)) \\ &\quad + 2(\varepsilon_e^v \varepsilon_e^a)^2 (s^2(\cos\theta(\cos\theta(\cos\theta(\cos\theta + 8) + 6) + 8) - 7) \\ &\quad \left. - 2m_X^2 s(\cos\theta + 1)(\cos\theta(5\cos\theta + 16) - 1) + 2m_X^4(\cos\theta(11\cos\theta + 26) + 7)) \right) \\ &\quad + \mathcal{O}\left(\left(\frac{m_e}{\sqrt{s}}\right)^2\right). \end{aligned} \quad (30)$$

The total cross section for the signal process is

$$\begin{aligned} \sigma_S &= \frac{4\pi\alpha^2}{3m_X^2 s(s + m_X^2)(s - m_X^2)^2} \\ &\quad (s((\varepsilon_e^v)^4 + (\varepsilon_e^a)^4)(3s^3 + 4m_X^2 s^2 + m_X^4 s - 6m_X^6) \\ &\quad + 2(\varepsilon_e^v)^2(\varepsilon_e^a)^2(3s^3 + 22m_X^2 s^2 - 5m_X^4 s - 18m_X^6)) \\ &\quad + 6((\varepsilon_e^v)^4 + (\varepsilon_e^a)^4 + 6(\varepsilon_e^v)^2(\varepsilon_e^a)^2)m_X^2(m_X^2 - s)(m_X^2 + s)^2 \log\left(\frac{m_X^2 + s}{m_X^2 - s}\right) \\ &\quad + \mathcal{O}\left(\left(\frac{m_e}{\sqrt{s}}\right)^2\right). \end{aligned} \quad (31)$$

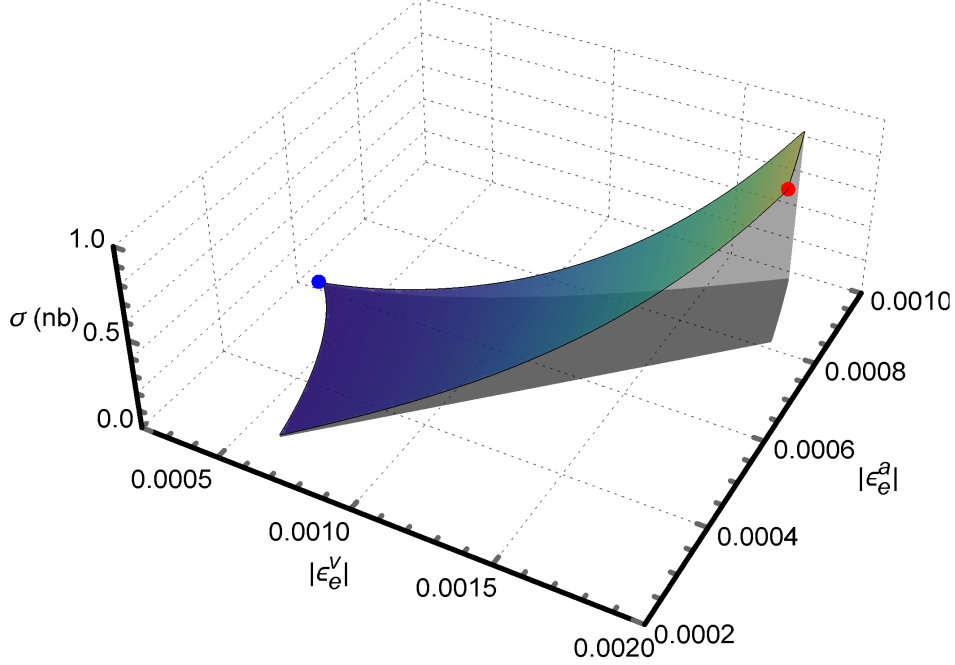


FIG. 4: The total cross section of the process $e^+e^- \rightarrow X \rightarrow e^+e^-$ as a function of the coupling parameters $|\varepsilon_e^v|$ and $|\varepsilon_e^a|$. The parameters $|\varepsilon_e^{v/a}|$ are constrained within the red region shown in Fig. 1. The red and blue spots denote the points corresponding to the maximum and minimum total cross section values, respectively.

In contrast to the background, both the differential and total cross sections for the signal process given by Eqs. (30) and (31) are highly reliable approximations.

In Fig. 4, we show the total cross section of the process $e^+e^- \rightarrow X \rightarrow e^+e^-$ as a function of the coupling parameters $|\varepsilon_e^v|$ and $|\varepsilon_e^a|$. The shaded area in the $|\varepsilon_e^v| - |\varepsilon_e^a|$ plane corresponds to the red constraint region in Fig. 1. The upper and lower limits of the total cross section are

$$0.011 \text{ nb} \lesssim \sigma(e^+e^- \rightarrow X \rightarrow e^+e^-) \lesssim 0.87 \text{ nb}, \quad (32)$$

where these limits correspond to the following coupling parameter values,

$$\begin{aligned} (|\varepsilon_e^v|, |\varepsilon_e^a|)_{\max}^{e^+e^- \rightarrow X \rightarrow e^+e^-} &\simeq (1.8, 0.82) \times 10^{-3}, \\ (|\varepsilon_e^v|, |\varepsilon_e^a|)_{\min}^{e^+e^- \rightarrow X \rightarrow e^+e^-} &\simeq (2.7, 6.1) \times 10^{-4}, \end{aligned} \quad (33)$$

which are identical to the coupling parameter values corresponding to the maximum and minimum $X \rightarrow e^+e^-$ decay widths in Eq. (26).

To gain a clearer understanding of the signal and background processes, we present the

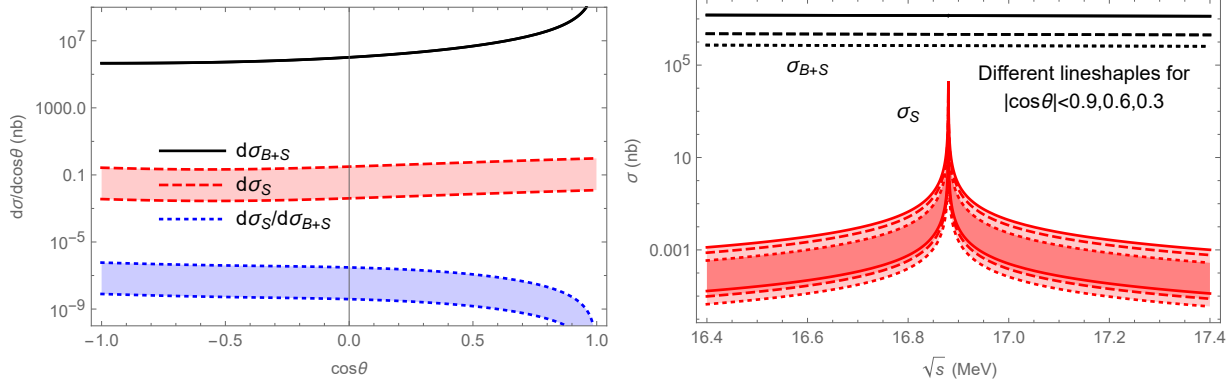


FIG. 5: Left panel: Differential cross section as a function of $\cos \theta$. Right panel: Total cross section as a function of \sqrt{s} . Here, σ_{B+S} includes the interference contribution between the background and signal processes, and the shaded area arises from the maximum and minimum coupling parameter values given in Eq. (33). In the right panel, the solid, dashed, and dotted lines correspond to the angular cuts $|\cos \theta| < 0.9$, $|\cos \theta| < 0.6$, and $|\cos \theta| < 0.3$, respectively.

differential and total cross sections for the $e^+e^- \rightarrow X/\gamma^* \rightarrow e^+e^-$ processes in Fig. 5. The left panel shows the differential distribution $d\sigma/d\cos\theta$, while the right panel displays the total cross section as a function of \sqrt{s} under three angular cuts. Here, θ denotes the angle between the outgoing electron and the colliding beams in the center-of-mass frame, σ_{B+S} includes the interference contribution between the background (B) and signal (S) processes, and the shaded area arises from the maximum and minimum coupling parameter values given in Eq. (33). In the left panel, it is evident that the differential cross section σ_{B+S} is more than seven orders of magnitude larger than the signal-only differential cross section σ_S . In the right panel, the solid, dashed, and dotted lines correspond to the angular cuts $|\cos \theta| < 0.9$, $|\cos \theta| < 0.6$, and $|\cos \theta| < 0.3$, respectively. It should be noted that sharper $X(17)$ peaks can be obtained in the right panel if smaller values of the $X(17)$ decay width Γ_X and a greater number of plotting points are used.

To identify the signal from the background, we further discuss the signal-to-noise ratio (SNR) around the $X(17)$ resonance peak. In Table I, we present the SNR, defined as $S/\sqrt{S+B}$ for the $e^+e^- \rightarrow X/\gamma^* \rightarrow e^+e^-$ processes under three angular cuts: $|\cos \theta| < 0.9$, $|\cos \theta| < 0.6$, and $|\cos \theta| < 0.3$. Values outside and inside the parentheses correspond to the maximum and minimum coupling parameter points given in Eq. (33), respectively. It

| $\cos\theta$ cuts | $ \cos\theta < 0.9$ | $ \cos\theta < 0.6$ | $ \cos\theta < 0.3$ |
|--------------------------|----------------------------------|----------------------------------|----------------------------------|
| Backgrounds (B) (mb) | 14 | 2.1 | 0.69 |
| Singnals (S) (nb) | 0.75(0.0094) | 0.44(0.0055) | 0.20(0.0025) |
| $S/\sqrt{S+B}$ | 0.00020 (2.5×10^{-6}) | 0.00030 (3.8×10^{-6}) | 0.00024 (3.0×10^{-6}) |

TABLE I: Signal-to-noise ratio ($S/\sqrt{S+B}$) for the $e^+e^- \rightarrow X/\gamma^* \rightarrow e^+e^-$ processes under three angular cuts: $|\cos\theta| < 0.9$, $|\cos\theta| < 0.6$, and $|\cos\theta| < 0.3$. Values outside and inside the parentheses correspond to the maximum and minimum coupling parameter points given in Eq. (33), respectively.

is found that the SNR is too small to detect $X(17)$ by measuring the total cross sections or counting events. Thus, we need to exploit observables that can identify the effects induced by the axial-vector component of the $V \pm A$ Xee coupling, since the background from Bhabha scattering only involves the pure vector coupling of the γee interaction.

IV. REVISITING $e^+e^- \rightarrow X(17)\gamma \rightarrow e^+e^-\gamma$ AT BESIII

In our previous work [26], we discussed the feasibility of searching for $X(17)$ in the $V - A$ model at the BESIII experiment, under the rough assumption that the coupling strengths are equal, $|\varepsilon_e^v| = |\varepsilon_e^a|$. Here, we revisit this search within the $V \pm A$ model, where the parameters $|\varepsilon_e^v|$ and $|\varepsilon_e^a|$ are constrained to the regions discussed in Sec. II C. In this section, we select the center-of-mass energy $\sqrt{s} = 3.773$ GeV. This choice is motivated by the fact that BESIII has collected a dataset of 20.275 ± 0.077 fb^{-1} at $\sqrt{s} = 3.773$ GeV [42], which is more than six times the size of the 3.083 fb^{-1} dataset at the J/ψ peak of $\sqrt{s} = 3.097$ GeV [43].

A. $X(17) + \gamma$ Production

Feynman diagrams for the production of the $X(17)$ boson in association with a photon in electron-positron collisions are presented in Fig. 6. At the BESIII experiment, the center-of-mass energy \sqrt{s} is much larger than the masses m_X and m_e ; additionally, the mass of

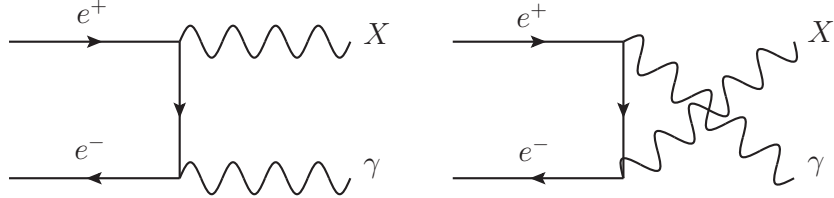


FIG. 6: The Feynman diagrams of the $X(17)$ boson production in association with a photon in electron-positron collisions.

$X(17)$ is much larger than that of the electron, $(\frac{m_e}{m_X})^2 \approx 0.1\%$. Under the “ $V \pm A$ ” model, we can thus derive a compact expression for the differential cross section,

$$\frac{d\sigma}{d\cos\theta} = \frac{2\pi\alpha^2}{s} ((\varepsilon_e^v)^2 + (\varepsilon_e^a)^2) \left(\frac{1 + \cos^2\theta}{1 - \cos^2\theta} \right) + \mathcal{O} \left(\left(\frac{m_e}{m_X} \right)^2, \left(\frac{m_X}{\sqrt{s}} \right)^2, \left(\frac{m_e}{\sqrt{s}} \right)^2 \right), \quad (34)$$

where θ is the angle between the outgoing photon and the beam axis. The complete differential cross section can be found in our previous works [26, 27]. We find that this approximation is sufficiently accurate, and it is difficult to distinguish it from the exact result in the BE-SIII energy region. Notably, the differential cross section is proportional to the combination $(\varepsilon_e^v)^2 + (\varepsilon_e^a)^2$ and exhibits singularities when the $X(17)$ boson propagates parallel to the beam axis at $|\cos\theta| = 1$.

The cross section of $e^+e^- \rightarrow X\gamma$ integrated over the angle is

$$\sigma = \frac{4\pi\alpha^2}{s} ((\varepsilon_e^v)^2 + (\varepsilon_e^a)^2) \left(\log \left[\frac{s}{m_e^2} \right] - 1 \right) + \mathcal{O} \left(\left(\frac{m_e}{m_X} \right)^2, \left(\frac{m_X}{\sqrt{s}} \right)^2, \left(\frac{m_e}{\sqrt{s}} \right)^2 \right). \quad (35)$$

The total cross section decreases as \sqrt{s} increases. Numerically, the approximated contribution in Eq. (35) is indistinguishable from the exact result. It is worth noting that the approximated contributions of the differential and total cross sections in Eqs. (34) and (35) are simply the differential and total cross sections of the $e^+e^- \rightarrow \gamma\gamma$ process multiplied by the factor $(\varepsilon_e^v)^2 + (\varepsilon_e^a)^2$, respectively.

In the left panel of Fig. 7, we display the normalized cross section $\sigma / ((\varepsilon_e^v)^2 + (\varepsilon_e^a)^2)$ for the process $e^+e^- \rightarrow X(17) + \gamma$ as a function of \sqrt{s} . The cross section at $\sqrt{s} = 3$ GeV is approximately 2.6 times that at $\sqrt{s} = 5$ GeV. In the right panel, we show the cross section for the process $e^+e^- \rightarrow X + \gamma$ as a function of the coupling parameters $|\varepsilon_e^v|$ and $|\varepsilon_e^a|$ at $\sqrt{s} = 3.773$ GeV. The shaded area in the $|\varepsilon_e^v| - |\varepsilon_e^a|$ plane corresponds to the viable

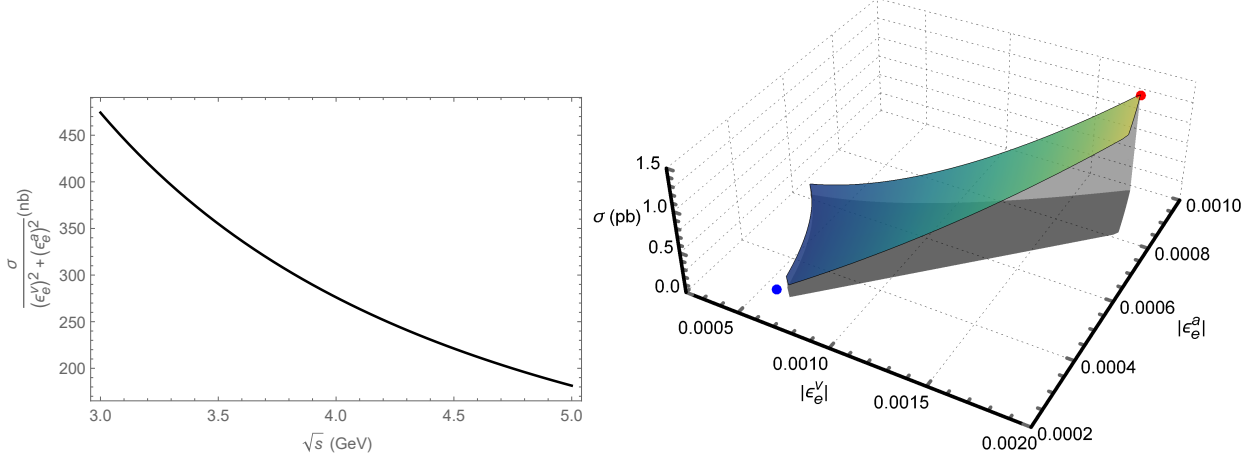


FIG. 7: Left panel: Normalized cross section $\sigma / ((\varepsilon_e^v)^2 + (\varepsilon_e^a)^2)$ (nb) for the process $e^+e^- \rightarrow X(17) + \gamma$ as a function of \sqrt{s} . Right panel: Cross section for the process $e^+e^- \rightarrow X(17) + \gamma$ as a function of the coupling parameters $|\varepsilon_e^v|$ and $|\varepsilon_e^a|$ at $\sqrt{s} = 3.773$ GeV. The parameters $|\varepsilon_e^{v/a}|$ are constrained within the red region shown in Fig. 1, where the red and blue spots denote the points corresponding to the maximum and minimum cross section values, respectively.

parameter space of $|\varepsilon_e^{v/a}|$ shown in Fig. 1. The upper and lower limits of the cross section are

$$0.14 \text{ pb} \lesssim \sigma(e^+e^- \rightarrow X\gamma) \lesssim 1.2 \text{ pb}, \quad (36)$$

which correspond to the following coupling parameter points,

$$\begin{aligned} (|\varepsilon_e^v|, |\varepsilon_e^a|)_{\max}^{e^+e^- \rightarrow X\gamma} &\simeq (1.7, 0.98) \times 10^{-3}, \\ (|\varepsilon_e^v|, |\varepsilon_e^a|)_{\min}^{e^+e^- \rightarrow X\gamma} &\simeq (6.1, 2.7) \times 10^{-4}. \end{aligned} \quad (37)$$

Using the 20.3 fb^{-1} dataset at $\sqrt{s} = 3.773$ GeV, and further considering that the BE-SIII detector covers about 93% solid angle, we can roughly estimate that there would be approximately $(2.6 \sim 23) \times 10^3$ $X(17)$ events.⁸

⁸ If we use the 3.083 fb^{-1} dataset at $\sqrt{s} = 3.097$ GeV, we would obtain $(0.57 \sim 5.1) \times 10^3$ $X(17)$ events, which are about one quarter of those at $\sqrt{s} = 3.773$ GeV.

B. $X(17)$ Reconstruction

In the laboratory frame of the $e^+e^- \rightarrow X\gamma$ process, the $X(17)$ boson travels relativistically with a velocity of $v = \frac{|\vec{p}_X|}{\sqrt{|\vec{p}_X|^2 + m_X^2}}$, where $|\vec{p}_X|$ is the three-dimensional momentum of $X(17)$ and satisfies $|\vec{p}_X| = E_\gamma = \frac{s-m_X^2}{2\sqrt{s}}$ with E_γ being the photon energy. At $\sqrt{s} = 3.773$ GeV, the velocity of $X(17)$ is $v = 0.99996c$. This relativistic motion extends the lifetime of $X(17)$ by approximately two orders of magnitude, resulting in a lifetime of $0.45 \sim 4.0$ ps. We then estimate the decay length of $X(17)$ in the detector as

$$L \approx (0.13 \sim 1.2) \text{ mm.} \quad (38)$$

This implies that $X(17)$ can be approximately assumed to be produced at the primary vertex inside the BESIII vacuum chamber. If we further consider that $X(17)$ decays into neutrinos or has some “dark” decay modes, the decay length would be even smaller.

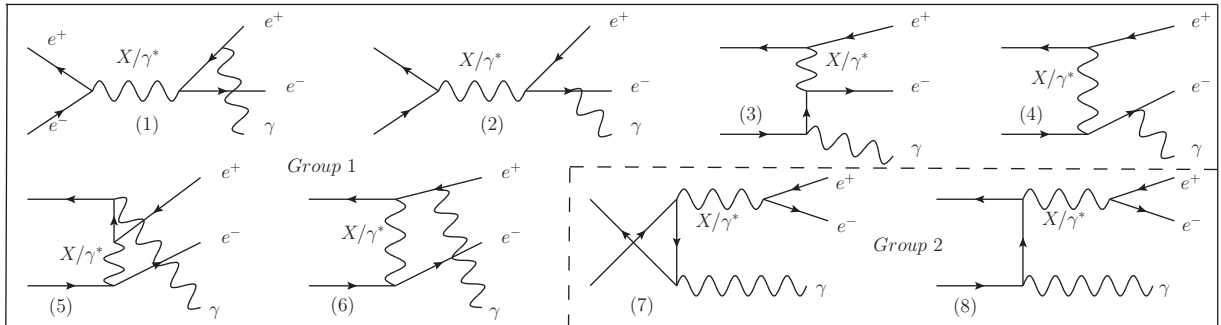


FIG. 8: Feynman diagrams for the process $e^+e^- \rightarrow e^+e^-\gamma$, involving both the $X(17)$ boson (signal) and virtual photon γ^* (background) as intermediates. In Diagrams (7, 8) of Group 2, the $X(17)$ boson decays directly into an electron-positron pair e^+e^- .

We proceed to discuss how to identify the $X(17)$ signals in the invariant mass spectrum $\sqrt{s_{ee}}$ of the final-state electron-positron pairs for the process $e^+e^- \rightarrow e^+e^-\gamma$. Feynman diagrams involving both the $X(17)$ boson (signal) and virtual photon (background) as intermediates are presented in Fig. 8, where the diagrams are categorized into two groups. The signal diagrams (7, 8) in Group 2 correspond to the process where the $X(17)$ boson decays directly into an electron-positron pair. These two diagrams will give rise to an $X(17)$ resonance bump in the invariant mass spectrum of the final-state electron-positron pairs. The differential cross section for the process $e^+(p_a)e^-(p_b) \rightarrow e^+(p_1)e^-(p_2)\gamma(p_3)$ can be formulated

as

$$d\sigma = \frac{(2\pi)^4}{4\sqrt{(p_a \cdot p_b)^2 - m_e^4}} \bar{\sum} |\mathcal{M}_{\text{sg}} + \mathcal{M}_{\text{bg}}|^2 d\Phi_3, \quad (39)$$

$$= \frac{1}{2(2\pi)^5 \sqrt{s(s - 4m_e^2)}} \bar{\sum} |\mathcal{M}_{\text{sg}} + \mathcal{M}_{\text{bg}}|^2 ds_{ee} dR_2(s, s_{ee}, 0) dR_2(s_{ee}, m_e^2, m_e^2), \quad (40)$$

with

$$dR_2(x, y, z) = \frac{\lambda^{\frac{1}{2}}(x, y, z)}{8x} d\Omega, \quad (41)$$

where $\bar{\sum}$ denotes the average over the initial spins and sum over the final spins, \mathcal{M}_{sg} and \mathcal{M}_{bg} are the amplitudes of the signal and background Feynman diagrams respectively, Φ_3 is the three-particle phase space, $s_{ee} = (p_1 + p_2)^2$, $\lambda(x, y, z) = (x - y - z)^2 - 4yz$, and Ω is the solid angle.

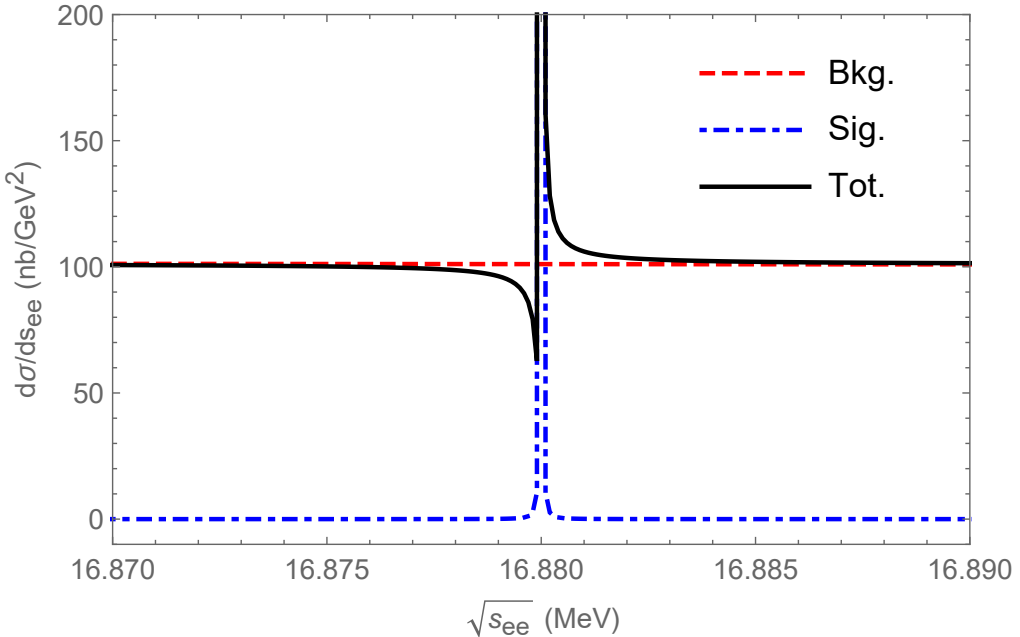


FIG. 9: Differential distribution $d\sigma/ds_{ee}$ of the process $e^+e^- \rightarrow e^+e^-\gamma$ near the $X(17)$ resonance peak, calculated for the maximum coupling parameter values $(|\varepsilon_e^v|, |\varepsilon_e^a|) = (1.7, 0.98) \times 10^{-3}$. The curves correspond to signal (blue dot-dashed curve), background (red dashed curve), and total contribution (black solid curve). BESIII experimental cuts are applied in the calculation.

In Fig. 9, we display the differential distribution of the process $e^+e^- \rightarrow e^+e^-\gamma$ as a function of the invariant mass $\sqrt{s_{ee}}$ near the $X(17)$ peak. The calculation uses the coupling parameter values $(|\varepsilon_e^v|, |\varepsilon_e^a|)_{\text{max}}^{e^+e^- \rightarrow X\gamma} \simeq (1.7, 0.98) \times 10^{-3}$, where the cross section of the

$e^+e^- \rightarrow X + \gamma$ process reaches its maximum. We find a remarkably sharp signal peak at $\sqrt{s_{ee}} = 16.88$ MeV, which decreases drastically to zero as $\sqrt{s_{ee}}$ deviates from the resonance peak. In other words, the Group 2 signal diagrams dominate near the resonance. This is attributed to the small decay width of $X(17)$ (given in Eq. (25)) in its Breit-Wigner propagator. For the total contribution, it lies consistently below the background curve before the resonance peak and above it after the peak. This behavior arises from the sign change of the interference contribution between the signal and background Feynman diagrams when crossing the resonance peak. Notably, to facilitate future comparisons with BESIII experiments, we have adopted the basic BESIII selection cuts [44] in Fig. 9,

$$|\cos \alpha| < 0.93 \quad \text{for electrons/positrons}, \quad (42)$$

$$|\cos \alpha| < 0.8 \quad \text{and} \quad E_\gamma > 25 \quad \text{MeV for photons in the barrel region}, \quad (43)$$

$$0.86 < |\cos \alpha| < 0.92 \quad \text{and} \quad E_\gamma > 50 \quad \text{MeV for photons in the endcap region}, \quad (44)$$

where α is the angle between the outgoing particles and the colliding beams.

To reconstruct the $X(17)$ signal in the invariant mass spectrum $\sqrt{s_{ee}}$ in the BESIII experiment, we need to consider the energy resolution of the BESIII detector around the 17 MeV region. The electromagnetic calorimeter (EMC) of BESIII exhibits the required performance, with an energy measurement range of 20 MeV to 2 GeV for electrons or photons. As shown in Fig. 33(a) of Ref. [45], its energy resolution is approximately 2.4% at 1 GeV, 3.3% at 100 MeV, and 9% at 20 MeV when using 5 cm \times 5 cm crystals. We assume that the energy resolution of $\delta(E)/E = 9\%$ is also a valid approximation in the $X(17)$ mass region, leading to an energy resolution of $\delta(17 \text{ MeV}) \approx 1.5 \text{ MeV}$. To enhance the robustness of the analysis, we consider three different energy resolution scenarios: 1 MeV, 1.5 MeV, and 3 MeV.

Due to the limited energy resolution of the BESIII detector, the $X(17)$ signal will not appear as the sharply prominent peak in the $\sqrt{s_{ee}}$ spectrum shown in Fig. 9. Instead, it will broaden into a Gaussian distribution with a mean value of m_X (the mass of $X(17)$) and a standard deviation equal to the energy resolution $\delta(m_X)$. For a Gaussian distribution, it is wellknown that 99.73% of the data points lie within three standard deviations (3σ) from the mean. In Table II, we estimate the signal events (S), background events (B), and signal-to-noise ratio (SNR, denoted $S/\sqrt{S+B}$) within the invariant mass ranges of $\sqrt{s_{ee}}$

| Energy resolution (MeV) | 1 | 1.5 | 3 |
|------------------------------|----------------|----------------|---------------|
| $\sqrt{s_{ee}}$ ranges (MeV) | [13.88, 19.88] | [12.38, 21.38] | [7.88, 25.88] |
| B ($\times 10^4$) | 42 | 64 | 139 |
| S ($\times 10^4$) | | 2.3 (0.26) | |
| $S/\sqrt{S+B}$ | 34(4.1) | 28 (3.3) | 19 (2.2) |

TABLE II: Signal events (S), background events (B), and signal-to-noise ratio ($S/\sqrt{S+B}$) in mass ranges deviating from the $X(17)$ signal bump by 3σ , for energy resolutions of 1 MeV, 1.5 MeV, and 3 MeV, and an integrated luminosity of 20.3 fb^{-1} . Values of S and $S/\sqrt{S+B}$ outside and inside the parentheses correspond to the maximum and minimum coupling parameter, respectively.

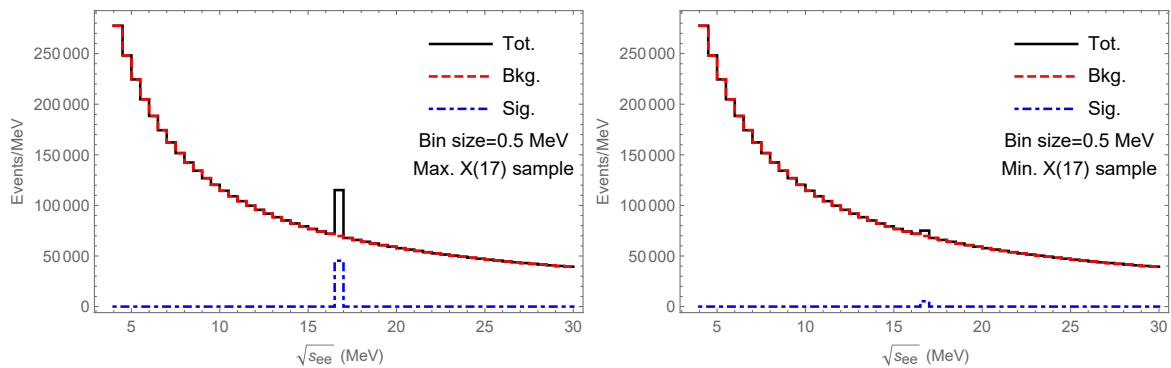


FIG. 10: Invariant mass spectrum distributions before smearing for the maximum and minimum $X(17)$ coupling parameter samples with a bin size of 0.5 MeV.

that are $\pm 3\sigma$ away from the sharp $X(17)$ peak. These estimates are performed for three different energy resolutions (1 MeV, 1.5 MeV, and 3 MeV) and an integrated luminosity of 20.3 fb^{-1} $\sqrt{s} = 3.773 \text{ GeV}$. Here, the background events are those exclusively within the three aforementioned $\sqrt{s_{ee}}$ ranges. Under the approximations of the saturated decay of $X \rightarrow e^+e^-$ and the tiny decay width of $X(17)$, we take the number of $X(17)$ events produced via the $e^+e^- \rightarrow X + \gamma$ process as the signal events. Additionally, the interference contribution between the signal and background is neglected because the cross sections below and above the sharp $X(17)$ peak are nearly symmetric, leading to mutual cancellation of the interference contribution. It is found that the SNR at the maximum coupling strength is promising for experimental detection, while it decreases by one order of magnitude at the

minimum coupling strength.

In Fig. 10, we present the invariant mass spectrum distributions before smearing for both the maximum and minimum $X(17)$ event samples with a bin size of 0.5 MeV. We find a distinct bump at $\sqrt{s_{ee}} = 16.88$ MeV for the maximum sample before smearing, while the height of the $X(17)$ bump for the minimum sample is approximately nine times lower. Naturally, the bumps would become sharper if a smaller bin size were adopted.

In Fig. 11, we present the invariant mass spectrum distributions after smearing for three energy resolutions, using both the maximum and minimum $X(17)$ event samples with a bin size of 0.5 MeV. The red solid curve, blue dashed curve, and black dotted curve correspond to energy resolutions of 1 MeV, 1.5 MeV, and 3 MeV, respectively. For the maximum $X(17)$ sample, the expected $X(17)$ bump is clearly observable with an energy resolution of 1 MeV. With the designed energy resolution of 1.5 MeV, the bump weakens into a shoulder; for an energy resolution of 3 MeV, this shoulder nearly disappears. To provide a clear view of the low-lying signal bump, we display the signal-only distribution as a subfigure in Fig. 11. It is worth noting that adjusting the bin size will not sharpen the bump after smearing. For the minimum $X(17)$ sample, the height of the bump is reduced by approximately ninefold, and the $X(17)$ signal cannot be distinguished from the background events. Thus, we may need to adopt appropriate kinematic cuts to improve the SNR.

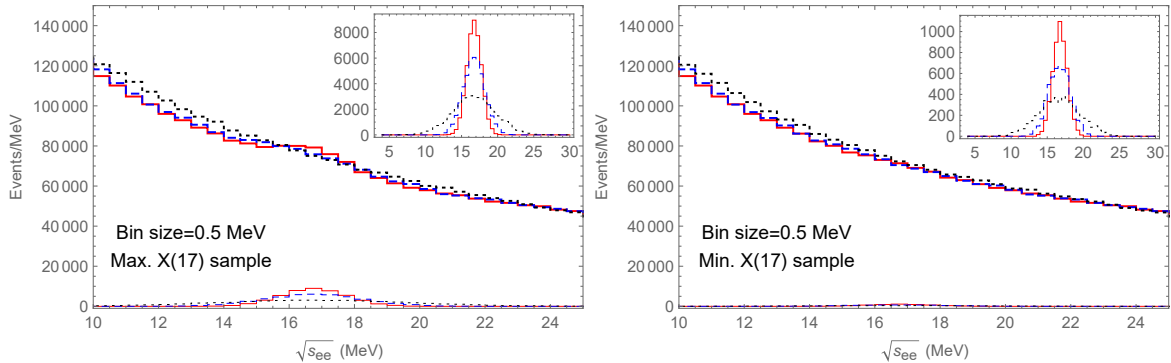


FIG. 11: Invariant mass spectrum distributions after smearing for the maximum and minimum $X(17)$ event samples, corresponding to energy resolutions of 1 MeV (red solid curve), 1.5 MeV (blue dashed curve), and 3 MeV (black dotted curve). Thick curves represent the sum of background and signal, while thin curves represent the signal only.

The subfigure shows the signal-only distribution.

V. SUMMARY AND PROSPECTS

Current experimental data indicate that only the $V \pm A$ interaction between $X(17)$ and electrons can explain the Atomki anomalies. We therefore extract constraints on the $V \pm A$ coupling of $X(17)$ to electrons from Atomki experiments, measurements of the electron anomalous magnetic moment, beam dump experiments, and the KLOE-2 experiment. To verify the new physics hypothesis, we discuss two experimental proposals for searching for $X(17)$: the $e^+e^- \rightarrow X(17) \rightarrow e^+e^-$ process at the PADME experiment, and the $e^+e^- \rightarrow X(17)\gamma \rightarrow e^+e^-\gamma$ process at the BESIII experiment. The signal-to-background ratio suggests that $X(17)$ signals are completely overwhelmed by background at the PADME experiment. However, observables capable of identifying the effects of the axial-vector component in the $V \pm A$ Xee coupling may exist, because the background from Bhabha scattering only involves the pure vector coupling of the γee interaction. Notably, it is promising to identify $X(17)$ signals in the $e^+e^- \rightarrow X(17)\gamma \rightarrow e^+e^-\gamma$ process at the BESIII experiment. Assuming the maximum coupling strength of the Xee interaction, a distinct $X(17)$ resonance appears in the invariant mass spectrum of the final e^+e^- pairs under reasonable detector resolution. Our results demonstrate that it is worthwhile for the BESIII experiment to attempt searching for the $X(17)$ particle via the $e^+e^- \rightarrow X(17)\gamma \rightarrow e^+e^-\gamma$ process using the 20 fb^{-1} dataset at $\sqrt{s} = 3.773 \text{ GeV}$.

What if no $X(17)$ signals are observed in new experiments beyond the several Atomki anomalies? In the latest PADME experiment [11], a bump at $\sqrt{s} = 16.90 \text{ MeV}$ with a significance of approximately 2σ is reported, and for the vector coupling hypothesis of the $X(17)$ boson, an upper limit of $|\varepsilon_e^v| \lesssim 5.6 \times 10^{-4}$ is obtained at the 90% C.L. Assuming the $V \pm A$ Xee interaction, we derive an upper limit of $(\varepsilon_e^v)^2 + (\varepsilon_e^a)^2 \lesssim 3.1 \times 10^{-7}$ at the 90% C.L. Further combining this constraint with those in Eq.(20), we find that there is no viable parameter space left for the $V \pm A$ $X(17)$ hypothesis. On the other hand, one may argue that the Atomki anomalies must originate from something unexpected, given that nuclear transitions involving excited ${}^8\text{Be}^*$, ${}^4\text{He}^*$, ${}^{12}\text{C}^*$, and GDR of ${}^8\text{Be}^*$ all indicate a resonance at the same mass position. In this case, the anomalies may stem from unrecognized nuclear effects. Could this be related to α -clusters? Notably, ${}^8\text{Be}$, ${}^4\text{He}$, and ${}^{12}\text{C}$ are all integer multiples of the α -particle (${}^4\text{He}$ nucleus), a characteristic feature that favors the formation

of α -cluster structures in these nuclei. This conjecture could be verified by searching for an unexpected bump in the electron-positron angular correlations during the de-excitation of the excited $^{16}\text{O}^*$ nucleus to its ground state, and by comparing these with those from the de-excitation of excited nuclei without α -cluster structures. Several appropriate excited states of $^{16}\text{O}^*$ lie around and above 17 MeV, as listed in Table 16.13 of Ref. [46]. To resolve this puzzle, more dedicated experiments are urgently required.

ACKNOWLEDGMENTS

We thank Prof. Jie Zhao who organized the workshop on $X(17)$ particle held in Fudan University on Aug. 11th, 2025. This work is supported in part by the National Key Research and Development Program of China under Contracts No. 2025YFA1613900, by the National Natural Science Foundation of China (NSFC) under the Grants 12475083, 12475087, 12235008.

[1] A. J. Krasznahorkay *et al.*, Phys. Rev. Lett. **116**, 042501 (2016), arXiv:1504.01527 [nucl-ex].

[2] A. J. Krasznahorkay *et al.*, J. Phys. Conf. Ser. **1056**, 012028 (2018).

[3] A. J. Krasznahorkay *et al.*, (2019), arXiv:1910.10459 [nucl-ex].

[4] A. J. Krasznahorkay, M. Csatlós, L. Csige, D. Firak, J. Gulyás, Á. Nagy, N. Sas, J. Timár, T. G. Tornyi, and A. Krasznahorkay, Acta Phys. Polon. B **50**, 675 (2019).

[5] A. J. Krasznahorkay, M. Csatlós, L. Csige, J. Gulyás, A. Krasznahorkay, B. M. Nyakó, I. Rajta, J. Timár, I. Vajda, and N. J. Sas, Phys. Rev. C **104**, 044003 (2021), arXiv:2104.10075 [nucl-ex].

[6] A. J. Krasznahorkay *et al.*, Phys. Rev. C **106**, L061601 (2022), arXiv:2209.10795 [nucl-ex].

[7] A. J. Krasznahorkay, A. Krasznahorkay, M. Csatlós, L. Csige, J. Timár, M. Begala, A. Krakó, I. Rajta, and I. Vajda, (2023), arXiv:2308.06473 [nucl-ex].

[8] A. J. Krasznahorky, A. Krasznahorkay, M. Csatlós, J. Timár, M. Begala, A. Krakó, I. Rajta, I. Vajda, and N. J. Sas, Universe **10**, 409 (2024), arXiv:2409.16300 [nucl-ex].

[9] F. Arias-Aragón, G. G. di Cortona, E. Nardi, and C. Toni, (2025), arXiv:2504.11439 [hep-ph].

- [10] K. Afanaciev et al. (MEG II), *Eur. Phys. J. C* **85**, 763 (2025), arXiv:2411.07994 [nucl-ex].
- [11] F. Bossi et al. (PADME), *JHEP* **11**, 007 (2025), arXiv:2505.24797 [hep-ex].
- [12] D. S. M. Alves et al., *Eur. Phys. J. C* **83**, 230 (2023).
- [13] J. L. Feng, B. Fornal, I. Galon, S. Gardner, J. Smolinsky, T. M. P. Tait, and P. Tanedo, *Phys. Rev. Lett.* **117**, 071803 (2016), arXiv:1604.07411 [hep-ph].
- [14] J. L. Feng, B. Fornal, I. Galon, S. Gardner, J. Smolinsky, T. M. P. Tait, and P. Tanedo, *Phys. Rev. D* **95**, 035017 (2017), arXiv:1608.03591 [hep-ph].
- [15] J. L. Feng, T. M. P. Tait, and C. B. Verhaaren, *Phys. Rev. D* **102**, 036016 (2020), arXiv:2006.01151 [hep-ph].
- [16] C.-Y. Wong, *JHEP* **08**, 165 (2020), arXiv:2001.04864 [nucl-th].
- [17] C.-Y. Wong and A. V. Koshelkin, *Eur. Phys. J. A* **59**, 285 (2023), arXiv:2111.14933 [hep-ph].
- [18] X. Zhang and G. A. Miller, *Phys. Lett. B* **773**, 159 (2017), arXiv:1703.04588 [nucl-th].
- [19] X. Zhang and G. A. Miller, *Phys. Lett. B* **813**, 136061 (2021), arXiv:2008.11288 [hep-ph].
- [20] A. C. Hayes, J. L. Friar, G. M. Hale, and G. T. Garvey, *Phys. Rev. C* **105**, 055502 (2022), arXiv:2106.06834 [nucl-th].
- [21] D. Banerjee et al. (NA64), *Phys. Rev. D* **101**, 071101 (2020), arXiv:1912.11389 [hep-ex].
- [22] L. Di Luzio, P. Paradisi, and N. Selimovic, *Nucl. Phys. B* **1021**, 117177 (2025), arXiv:2504.14014 [hep-ph].
- [23] N. V. Krasnikov, *Mod. Phys. Lett. A* **35**, 2050116 (2020), arXiv:1912.11689 [hep-ph].
- [24] R. H. Parker, C. Yu, W. Zhong, B. Estey, and H. Müller, *Science* **360**, 191 (2018), arXiv:1812.04130 [physics.atom-ph].
- [25] D. Barducci and C. Toni, *JHEP* **02**, 154 (2023), [Erratum: *JHEP* 07, 168 (2023)], arXiv:2212.06453 [hep-ph].
- [26] J. Jiang, L.-B. Chen, Y. Liang, and C.-F. Qiao, *Eur. Phys. J. C* **78**, 456 (2018).
- [27] J. Jiang, H. Yang, and C.-F. Qiao, *Eur. Phys. J. C* **79**, 404 (2019), arXiv:1810.05790 [hep-ph].
- [28] R. Aliberti et al., *Phys. Rept.* **1143**, 1 (2025), arXiv:2505.21476 [hep-ph].
- [29] D. P. Aguillard et al. (Muon g-2), *Phys. Rev. Lett.* **135**, 101802 (2025), arXiv:2506.03069 [hep-ex].
- [30] D. R. Tilley, J. H. Kelley, J. L. Godwin, D. J. Millener, J. E. Purcell, C. G. Sheu, and H. R. Weller, *Nucl. Phys. A* **745**, 155 (2004).
- [31] J. Gulyás, T. J. Ketel, A. J. Krasznahorkay, M. Csatlós, L. Csige, Z. Gácsi, M. Hunyadi,

A. Krasznahorkay, A. Vitéz, and T. G. Tornyi, Nucl. Instrum. Meth. A **808**, 21 (2016), arXiv:1504.00489 [nucl-ex].

[32] X. Fan, T. G. Myers, B. A. D. Sukra, and G. Gabrielse, Phys. Rev. Lett. **130**, 071801 (2023), arXiv:2209.13084 [physics.atom-ph].

[33] D. Hanneke, S. Fogwell, and G. Gabrielse, Phys. Rev. Lett. **100**, 120801 (2008), arXiv:0801.1134 [physics.atom-ph].

[34] J. P. Leveille, Nucl. Phys. B **137**, 63 (1978).

[35] D. Banerjee et al. (NA64), Phys. Rev. Lett. **120**, 231802 (2018), arXiv:1803.07748 [hep-ex].

[36] E. Depero et al. (NA64), Eur. Phys. J. C **80**, 1159 (2020), arXiv:2009.02756 [hep-ex].

[37] Y. M. Andreev et al. (NA64), Phys. Rev. D **104**, L111102 (2021), arXiv:2104.13342 [hep-ex].

[38] J. D. Bjorken, R. Essig, P. Schuster, and N. Toro, Phys. Rev. D **80**, 075018 (2009), arXiv:0906.0580 [hep-ph].

[39] A. Rohatgi, “Webplotdigitizer,” .

[40] S. Andreas, C. Niebuhr, and A. Ringwald, Phys. Rev. D **86**, 095019 (2012), arXiv:1209.6083 [hep-ph].

[41] A. Anastasi et al., Phys. Lett. B **750**, 633 (2015), arXiv:1509.00740 [hep-ex].

[42] M. Ablikim et al. (BESIII), Chin. Phys. C **48**, 123001 (2024), arXiv:2406.05827 [hep-ex].

[43] M. Ablikim et al. (BESIII), Chin. Phys. C **46**, 074001 (2022), arXiv:2111.07571 [hep-ex].

[44] M. Ablikim (BESIII), Phys. Rev. D **93**, 052005 (2016), arXiv:1510.01641 [hep-ex].

[45] M. Ablikim et al. (BESIII), Nucl. Instrum. Meth. A **614**, 345 (2010), arXiv:0911.4960 [physics.ins-det].

[46] D. R. Tilley, H. R. Weller, and C. M. Cheves, Nucl. Phys. A **564**, 1 (1993).